ACS APPLIED MATERIALS & INTERFACES

www.acsami.org

Research Article

Ultrafast Reactive Laser Sintering of Highly Conductive Garnet-Type LLZTO Solid Electrolytes

Erika P. Ramos,* Yudan Chen, Aaron Santomauro, Yan-Yan Hu, Samuel Sanghyun Lee, Jianhua Tong, and Jianchao Ye*

Cite This: *ACS Appl. Mater. Interfaces* 2026, 18, 37654–37665

Read Online

ACCESS | Metrics & More | Article Recommendations | Supporting Information

ABSTRACT: Rapid and scalable fabrication of garnet-type solid electrolytes remains a major challenge for the practical deployment of lithium metal batteries. Here, we report reactive laser sintering (RLS) as an ultrafast and potentially scalable strategy for fabricating garnet-type $Li_{6.4}La_3Zr_{1.4}Ta_{0.6}O_{12}$ (LLZTO) solid electrolytes. RLS of LLZTO enables simultaneous reaction and densification, achieving ~95% relative density while minimizing lithium loss and suppressing secondary phase formation. Compared to conventional furnace sintering, RLS promotes enhanced grain growth and improved densification, leading to improved ionic conductivity (0.36 ± 0.08 mS cm^{-1}) while maintaining comparable activation energies for Li^+ transport. Structural characterization by X-ray diffraction (XRD), Raman spectroscopy, and solid-state $^6Li/^7Li$ NMR confirms the formation of cubic garnet LLZTO with homogeneous microscale elemental distribution. In addition, nanoindentation measurements demonstrate that RLS preserves the mechanical properties of the garnet framework despite ultrafast localized thermal processing. By integrating simultaneous reaction and densification with tunable microstructural control, reactive laser sintering provides a promising manufacturing pathway for high-performance garnet solid electrolytes toward next-generation solid-state batteries.

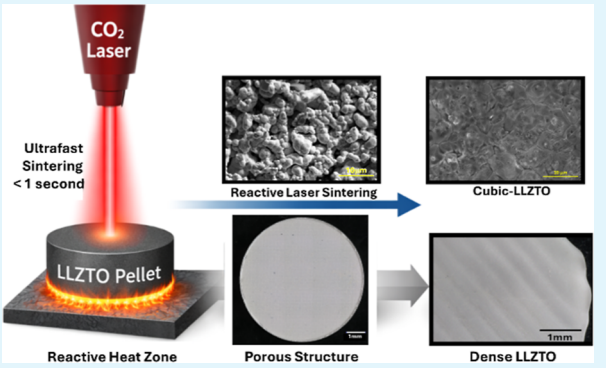

KEYWORDS: *reactive laser sintering, garnet solid electrolytes, solid-state batteries, ultrafast densification, CO_2 laser*

1. INTRODUCTION

Solid-state batteries (SSBs) are widely regarded as a promising next-generation energy storage technology because they offer improved safety and higher energy density than conventional lithium-ion batteries (LIBs).[1,2] These advantages arise from the use of nonflammable solid electrolytes and compatibility with lithium metal anodes, which possess an exceptionally high theoretical capacity (~3861 mAh g^{-1}) and low redox potential (~−3.04 V vs SHE).[3,4] Together, these features enable substantially higher gravimetric and volumetric energy densities than conventional graphite-based LIBs, with projected values exceeding ~500 Wh kg^{-1} and ~1000 Wh L^{-1} in practical cell configurations.[5,6] In addition, replacing flammable liquid electrolytes with solid-state electrolytes significantly improves operational safety by mitigating thermal runaway risks, which is particularly important for large-format and high-energy applications.[6,7]

Realizing these performance gains requires solid-state electrolytes that not only exhibit high ionic conductivity and electrochemical stability, but can also be fabricated by scalable, cost-effective manufacturing routes suitable for large-area production.[8,9] Compared with sulfide-based electrolytes (e.g., $Li_2S-P_2S_5$)[10−12] and argyrodites (Li_6PS_5X)[13−15] with high ionic conductivity but narrow electrochemical stability window, oxide-based $Li_7La_3Zr_2O_{12}$ (LLZO)[16] and its doped derivatives (Nb, Ta,[17] Ga, and Al)[18−20] remain attractive because of their superior chemical robustness,[21] broader electrochemical stability window with enhanced compatibility with both lithium metal and high-voltage cathodes.[22,23] These characteristics position LLZO among the most promising solid electrolytes for practical solid-state battery applications.

Despite these advantages, scalable fabrication of dense LLZO remains a major challenge.[24] Conventional high-temperature sintering (>1000 °C) typically requires prolonged dwell times, which promote lithium volatilization, nonuniform densification[25] grain-boundary resistance, and secondary phase formation such as $La_2Zr_2O_7$.[26,27] Recent reviews have identified densification control, lithium retention, and interface stability as key bottlenecks for practical oxide solid electrolytes.[26,28,29] Recent studies have shown that lithiophilic and electron-blocking interlayers can improve lithium wettability

Received: March 14, 2026
Revised: June 26, 2026
Accepted: June 29, 2026
Published: July 6, 2026

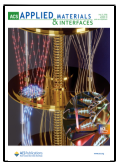

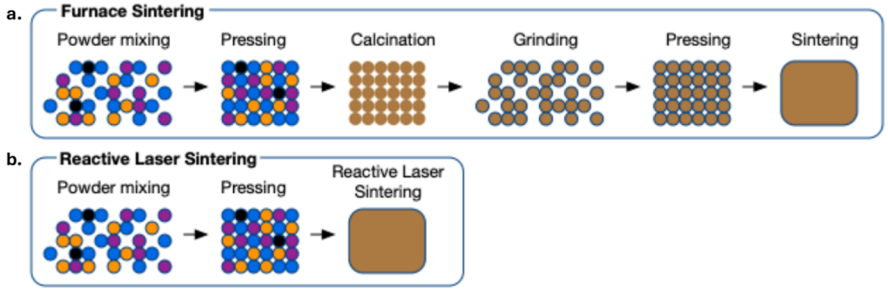

Figure 1. Schematic comparison of LLZTO ceramic electrolyte fabrication: (a) conventional multistep sintering involving repeated pelletization, calcination, and grinding; and (b) reactive laser sintering, which streamlines the process with fewer synthesis steps.

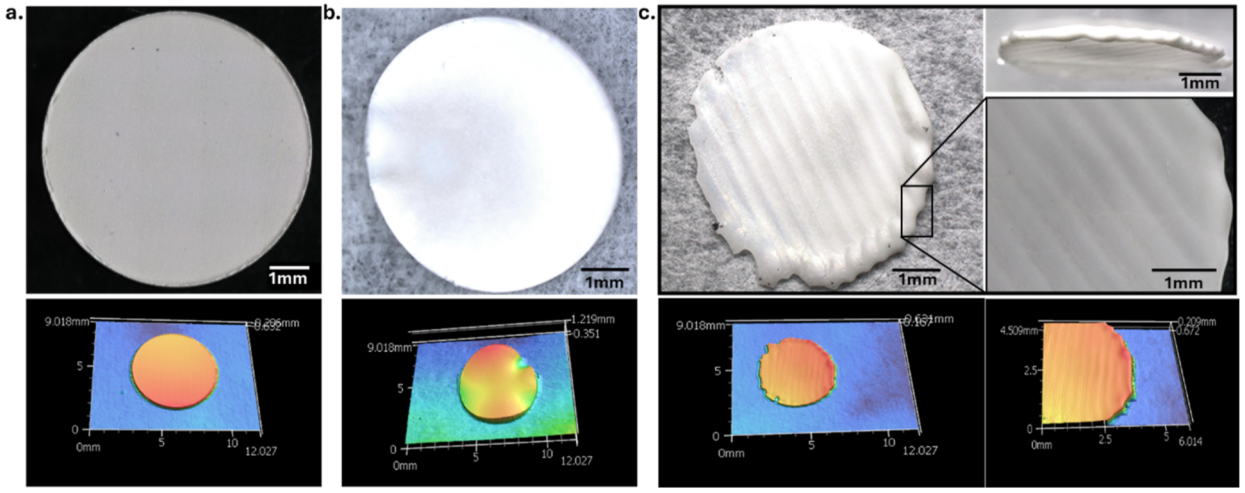

Figure 2. Macroscopic images and surface profiles of (a) pristine; (b) furnace-sintered, and (c) reactive laser sintered LLZTO pellets.

and suppress interfacial side reactions under stack pressure conditions,[30,31] while scalable membrane fabrication approaches such as tape casting have enabled the production of dense garnet membranes for large-area solid-state battery architectures.[32] These studies collectively demonstrate that both microstructural control and interfacial engineering are essential for practical implementation of LLZO-based electrolytes.

Considerable effort has therefore been devoted to developing alternative densification strategies capable of reducing thermal budgets while preserving lithium stoichiometry and achieving high relative density.[33−35] Approaches including reactive sintering from pyrochlore precursors,[36,37] molten-salt synthesis,[38,39] oxygen-assisted sintering,[40,41] hot pressing,[42] cold sintering,[40,41] and tape-casting-based rapid sintering routes[43] have all demonstrated improved densification and microstructural control. More recently, ultrafast densification strategies such as spark plasma sintering (SPS),[44−46] ultrafast high-temperature sintering (UHS),[47−49] flash sintering,[25,50,51] and Joule-heating-assisted processing[25,52] have demonstrated dramatic reductions in processing time and thermal exposure for garnet electrolytes.[44,45,53,54] SPS[51] and hot-pressing methods can achieve high density and reduced grain-boundary resistance; however, these approaches typically require external pressure and conductive graphite tooling, limiting scalability and geometric flexibility.[46,54] Flash sintering and Joule-heating-assisted methods enable densification within seconds but often rely on electric-field activation, conductive architectures, or presynthesized LLZO powders. Consequently, many rapid densification strategies still decouple garnet phase formation from densification,[23,55] requiring separately synthesized LLZO powders prior to consolidation and maintaining energy-intensive precursor synthesis routes.[29,56,57]

In contrast, laser-based processing offers a pressureless and spatially selective route capable of generating highly localized heating with extremely high heating and cooling rates. Such localized thermal profiles can promote rapid densification while minimizing prolonged thermal exposure and lithium volatilization. In addition, the extreme thermal gradients and transient localized melting generated during laser exposure may enable rapid mass transport and melt-assisted densification pathways that are fundamentally distinct from equilibrium furnace-based processing. Such characteristics are particularly attractive for scalable and digitally controlled manufacturing of ceramic solid electrolytes. Building on this concept, we previously demonstrated ultrafast CO_2 laser sintering of presynthesized LLZTO films within 1 s, achieving ∼95.7% relative density and ionic conductivity of 0.26 mS cm^{-1}.[58] However, most reported laser-based approaches still rely on presynthesized LLZO powders and therefore do not fully integrate phase formation and densification into a single processing step.

Here, we address these limitations through reactive laser sintering (RLS), a pressureless ultrafast processing strategy in which LLZTO precursors undergo simultaneous garnet phase formation and densification under highly localized laser heating in a controlled atmosphere. The resulting RLS LLZTO exhibits ∼95% relative density and enhanced ionic conductivity (0.36 mS cm^{-1}), while minimizing prolonged lithium volatilization. Structural and chemical characterization using

https://doi.org/10.1021/acsami.6c05262
ACS Appl. Mater. Interfaces 2026, 18, 37654−37665

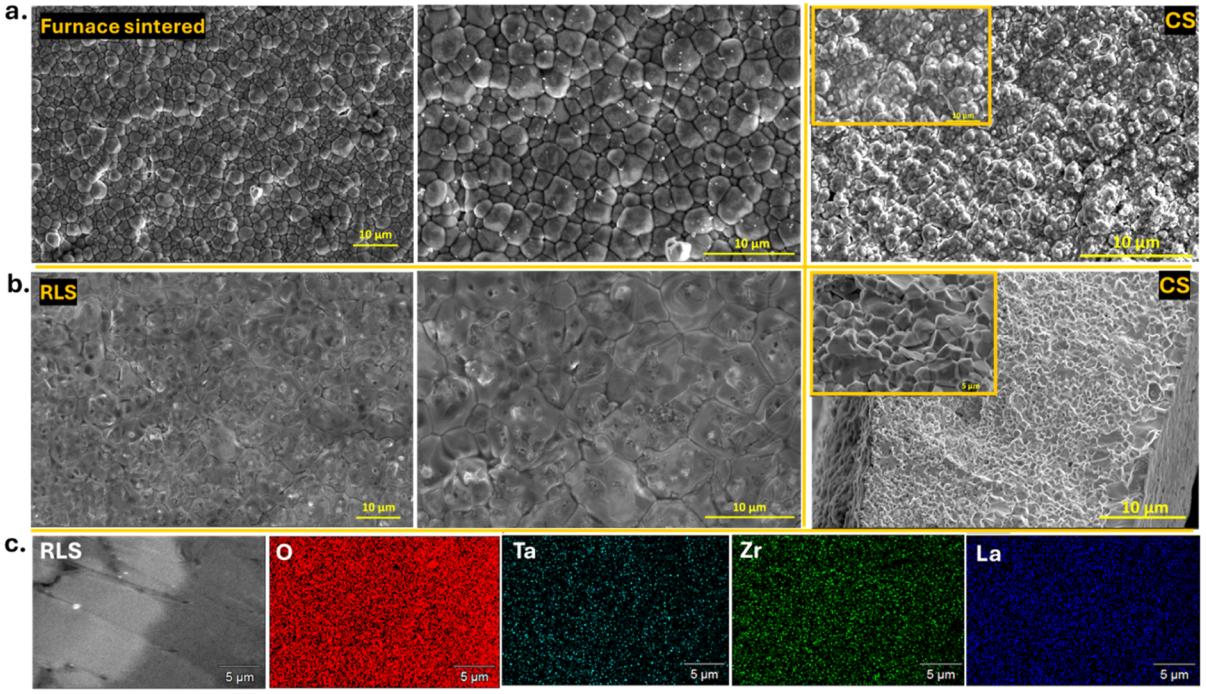

Figure 3. Microstructural characterization of LLZTO samples. SEM images of (a) furnace-sintered; (b) CO_2 reactive laser sintering LLZTO using an areal laser energy density of 1.67 J mm^{-2}, showing top-view and cross-sectional morphologies; and (c) EDS elemental maps of La, Zr, and Ta in an ion-polished RLS LLZTO cross-section.

X-ray diffraction (XRD), Raman spectroscopy, solid-state ^{6}Li/^{7}Li NMR, and scanning electron microscopy (SEM) confirms cubic garnet formation, dense microstructures, and overall microscale compositional homogeneity. Direct comparison with conventionally furnace-sintered counterparts demonstrates that reactive laser sintering provides a rapid, scalable, and compositionally integrated pathway for manufacturing highly conductive garnet solid electrolytes.

2. RESULTS AND DISCUSSION

A clear contrast exists between the traditional multistep fabrication of LLZTO ceramic electrolytes and the streamlined reactive laser sintering approach. Conventional processing typically involves repeated cycles of pelletization, calcination, and grinding or ball milling (Figure 1a), often performed multiple times to achieve the high density and ionic conductivity required for practical applications. These routes are time- and energy-intensive and can induce lithium loss, secondary phase formation, and significant challenges in scaling to large-area or high-throughput manufacturing. By contrast, reactive laser sintering, as shown in Figure 1b, offers a compelling alternative to conventional furnace sintering for LLZTO electrolytes. This method enables ultrafast sintering with subsecond dwell times, promotes high densification, mitigates lithium volatilization, and integrates phase formation and densification into a single processing step. To benchmark ultrafast reactive laser sintering (RLS) against conventional furnace sintering, ball-milled (BM) LLZTO precursors were pelletized and processed at 1100 °C for 6 h in a box furnace (Experimental Section).

Figure 2 compares the microscopic appearance and surface profiles of pristine, furnace-sintered, and RLS-sintered LLZTO pellets. The pristine pellet (Figure 2a) is smooth and mechanically intact, with a diameter of ∼6.3 mm and a flat surface confirmed by optical profilometry. After furnace sintering (Figure 2b), the pellet diameter decreases to ∼5.92 mm and exhibits noticeable surface deformation, as revealed by profilometry. This behavior likely arises from nonuniform shrinkage during prolonged thermal treatment at 1100 °C for 6 h, leading to heterogeneous densification across the pellet.

Unlike furnace sintering, which involves long-duration bulk heating with high cumulative thermal energy input, RLS operates under highly localized and transient energy delivery conditions characterized by high areal energy density. RLS LLZTO pellet (Figure 2c) was processed using an areal energy density (AED = P/hu) of 1.67 J mm^{-2} under a 2 W CO_2 laser power (P), with a 1.5 mm (e^{-2}) Gaussian beam diameter, scan speed (u) of 4 mm s^{-1}, and hatch spacing (h) of 0.3 mm. These parameters were selected based on prior optimization in LLZTO CO_2 laser sintering studies, where comparable energy densities enabled rapid densification under ultrafast thermal conditions.[58] The RLS pellet shows a reduction in diameter from ∼6.0 mm to ∼5.5 mm, primarily attributed to localized edge rounding and minor material redistribution at the pellet perimeter during laser scanning. Despite this peripheral effect, the sample undergoes rapid densification within subsecond time scales and develops a glossy, laser-textured surface.

Surface profilometry reveals a periodic, wave-like morphology with an average amplitude of ∼0.2 mm, consistent with previously reported laser-processed LLZTO structures.[58] This surface modulation originates from the Gaussian energy distribution of the CO_2 laser beam, the line-by-line scanning strategy, and rapid melt−quench dynamics during processing. Localized differences in energy density across each scan track lead to preferential sintering/melting at the beam center and differential shrinkage, resulting in a characteristic groove-like morphology. Similar features have also been observed in our previous work on nonreactive laser sintering of LLZTO. This laser-induced 3D surface topology may influence interfacial contact behavior in solid-state battery assemblies by modifying

https://doi.org/10.1021/acsami.6c05262
ACS Appl. Mater. Interfaces 2026, 18, 37654−37665

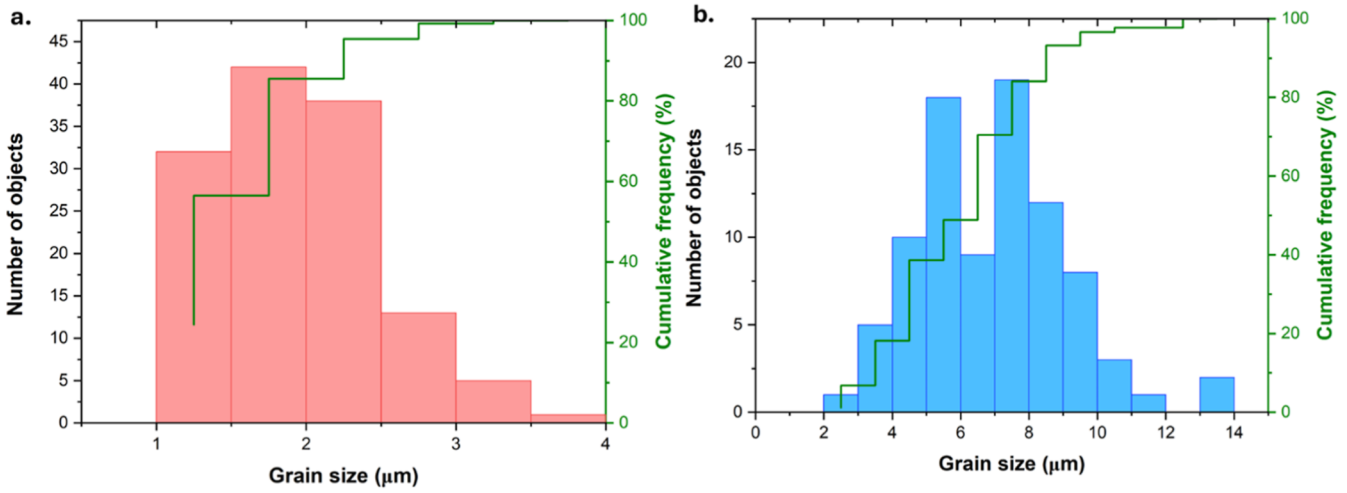

Figure 4. Histograms of (a) furnace-sintered LLZTO; and (b) reactive laser sintering LLZTO, showing the distribution of grain sizes.

the effective contact area at solid−solid interfaces. In this context, increased surface roughness could be beneficial by enhancing interfacial contact and potentially reducing local current density. The 3D wavy surface morphology may enhance contact with electrode layers, potentially reducing effective current density and aligning with emerging concepts in three-dimensional solid-state battery architectures.[59,60]

Importantly, these surface features are not inherent limitations of the RLS process and can be tuned through laser parameters such as beam shaping, spot size, raster spacing, and scan speed, or further modified via postprocessing strategies including surface planarization or interfacial coating deposition. Overall, the observed morphology reflects a controllable outcome of the laser processing window, highlighting the distinct densification and surface evolution pathways enabled by reactive laser sintering compared with conventional furnace processing.

To further probe the microstructural differences induced by the sintering pathway, the samples were characterized by scanning electron microscopy (SEM), with emphasis on grain morphology and grain-boundary density. Figure 3 presents top-view and cross-sectional SEM images of furnace-sintered and RLS LLZTO (AED: 1.67 J mm^{-2}). The furnace-sintered sample (Figure 3a) exhibits a relatively uniform fine-grained microstructure with closely packed grains and well-defined grain boundaries, characteristic of conventionally sintered LLZTO ceramics. In contrast, the RLS LLZTO (Figure 3b) displays significantly larger grains and a reduced grain-boundary density. Although the overall microstructure remains highly dense, the grain boundaries appear less distinct, and localized surface features or void-like regions are observed, likely arising from the rapid solidification and localized melt−quench dynamics associated with laser processing.

These differences reflect the fundamentally distinct thermal conditions enabled by RLS, where extremely high heating and cooling rates generate steep thermal gradients and transient localized melting at particle interfaces. Consistent with previous reports on laser sintering of ceramics,[61,62] such transient melt-assisted sintering enhances mass transport and grain-boundary mobility, promoting rapid pore elimination, grain coarsening, and densification within subsecond processing times. Simultaneously, rapid quenching suppresses prolonged diffusion and preserves nonequilibrium microstructural features formed during laser exposure.

Figure 3c shows EDS elemental mapping of an ion-polished RLS LLZTO cross-section, revealing an overall homogeneous distribution of La, Zr, and Ta throughout the microstructure. Quantitative EDS analysis (Figure S1) further indicates that the elemental composition is generally consistent with the nominal LLZTO garnet stoichiometry, with an approximate composition of Zr ≈ 1.54, La ≈ 2.70, Ta ≈ 0.76, and O ≈ 10.9 per formula unit.

Grain size analysis further highlights the influence of the sintering pathway on microstructural evolution. The furnace-sintered sample exhibits a smaller average grain size of 1.954 ± 0.556 μm (Figure 4a), whereas the RLS LLZTO displays a significantly larger average grain size of 5.833 ± 2.445 μm (Figure 4b), indicating enhanced grain growth under rapid laser sintering conditions. This pronounced coarsening in the RLS sample is attributed to the intense localized heating and steep thermal gradients generated during laser exposure, which accelerate atomic diffusion and grain-boundary mobility.[63−65]

The densification mechanism in RLS can be described as a hybrid process involving transient liquid-phase-assisted sintering and accelerated solid-state diffusion.[66,67] Under intense CO_2 laser irradiation, localized surface and interparticle melting occurs, forming short-lived liquid films at particle contacts. These transient liquid regions enhance capillary-driven mass transport, promoting rapid neck formation, pore elimination, and densification within subsecond time scales.[68] Concurrently, steep thermal gradients and high peak temperatures promote accelerated solid-state diffusion in surrounding regions. The combination of these processes enables rapid grain growth and densification, while quenching freezes the evolved microstructure, preserving the resulted large-grained, highly dense morphology characteristic of RLS-processed LLZTO.

To further evaluate densification, representative samples from each processing route were ion-milled and analyzed by SEM cross sections using ImageJ to estimate porosity and relative density (Figure S2). The furnace-sintered LLZTO exhibits a porosity of 15.46 ± 1.96%, whereas the RLS sample shows a substantially lower porosity of 4.76 ± 0.27%, corresponding to a relative density of ∼95%. The comparatively lower density of the furnace-sintered sample relative to

https://doi.org/10.1021/acsami.6c05262
ACS Appl. Mater. Interfaces 2026, 18, 37654−37665

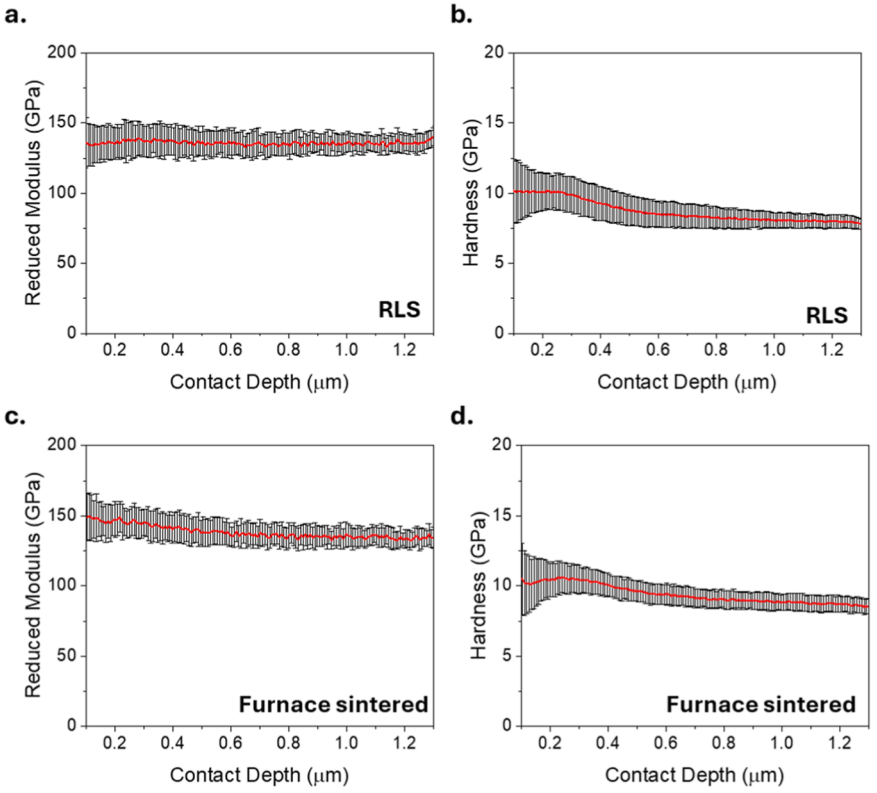

Figure 5. Nanoindentation-derived mechanical properties comparing the reduced modulus and hardness values of both samples of (a,b): reactive laser sintered LLZTO sample, and (c,d) furnace sintered LLZTO sample.

typical literature values (>90−95% at ∼1100 °C) may arise from the small pellet dimensions used in this study (<1 cm diameter and ∼500 μm thickness), which increase the surface-area-to-volume ratio and promote lithium volatilization during prolonged high-temperature sinterin.[69,70] In contrast, the rapid RLS process enables efficient densification while minimizing lithium loss. It should be noted that porosity values derived from SEM cross sections may be influenced by localized sampling effects, particularly given the textured surface morphology of the RLS samples. To reduce this uncertainty, multiple representative cross-sectional regions were analyzed and averaged. Nevertheless, complementary bulk density measurements, such as Archimedes analysis, would provide additional validation and will be explored in future studies.

The mechanical properties of the RLS and furnace-sintered LLZTO samples were measured by nanoindentation (Figure 5). The RLS LLZTO exhibits a reduced modulus of 135.6 ± 6.2 GPa and a hardness of 8.08 ± 0.2 GPa at 1 μm contact depth, while the furnace-sintered sample shows comparable modulus of 134.8 ± 6.9 GPa and slightly higher hardness of 8.87 ± 0.2 GPa, respectively. The possible hardness reduction may arise from rapid sintering induced residual stress, which is described later in the X-ray diffraction (XRD) analysis. Overall, these results indicate that ultrafast reactive laser sintering preserves the mechanical integrity of the garnet framework while enabling rapid densification under localized thermal conditions.

The furnace-sintered and RLS LLZTO samples were characterized by X-ray diffraction (XRD) to examine their phase composition and crystallographic structure. Figure 6a presents the XRD patterns of the ball-milled (BM) LLZTO precursors, the RLS-processed sample, and the furnace-sintered counterpart, with all Bragg reflections indexed to the cubic garnet phase (c-LLZTO). As expected, the high-energy wet-milled precursors exhibit residual unreacted phases, as shown in Figure S3. In contrast, both sintered samples display diffraction patterns consistent with the cubic LLZTO structure, confirming successful phase formation after sintering. Figure 6b shows the XRD pattern and Rietveld refinement of the RLS LLZTO processed at an areal energy density (AED) of 1.67 J mm^{-2}, with the corresponding crystallographic parameters summarized in Table 1. The refinement confirms the formation of phase-pure cubic LLZTO, demonstrating the capability of reactive laser sintering to simultaneously induce phase formation and densification within ultrafast (<1 s) processing times. To investigate the influence of laser energy input on the LLZTO phase evolution and crystallographic ordering, the laser scan speed was decreased from 4 mm s^{-1} to 3 mm s^{-1}, increasing the AED from 1.67 to 2.22 J mm^{-2}. As shown in Figure 6c this increase in energy density produces noticeable changes in the diffraction pattern. In particular, the intensities of the (211) and (321) reflections decrease, the (022) reflection disappears, and the (004) reflection becomes more pronounced relative to both the lower-AED RLS sample and the furnace-sintered LLZTO (Figure 6b,d). These changes suggest that higher laser energy densities influence crystallographic texture and structural ordering during rapid laser processing.

At the higher AED (2.22 J mm^{-2}), a $La_2Zr_2O_7$ secondary phase (∼9.23 wt %) is also detected, likely due to partial garnet decomposition under highly localized and nonequilibrium thermal conditions. Complementary SEM analysis (inset Figures 6c and S4) reveals a densely sintered microstructure consisting of coalesced faceted grains with localized surface

https://doi.org/10.1021/acsami.6c05262
ACS Appl. Mater. Interfaces 2026, 18, 37654−37665

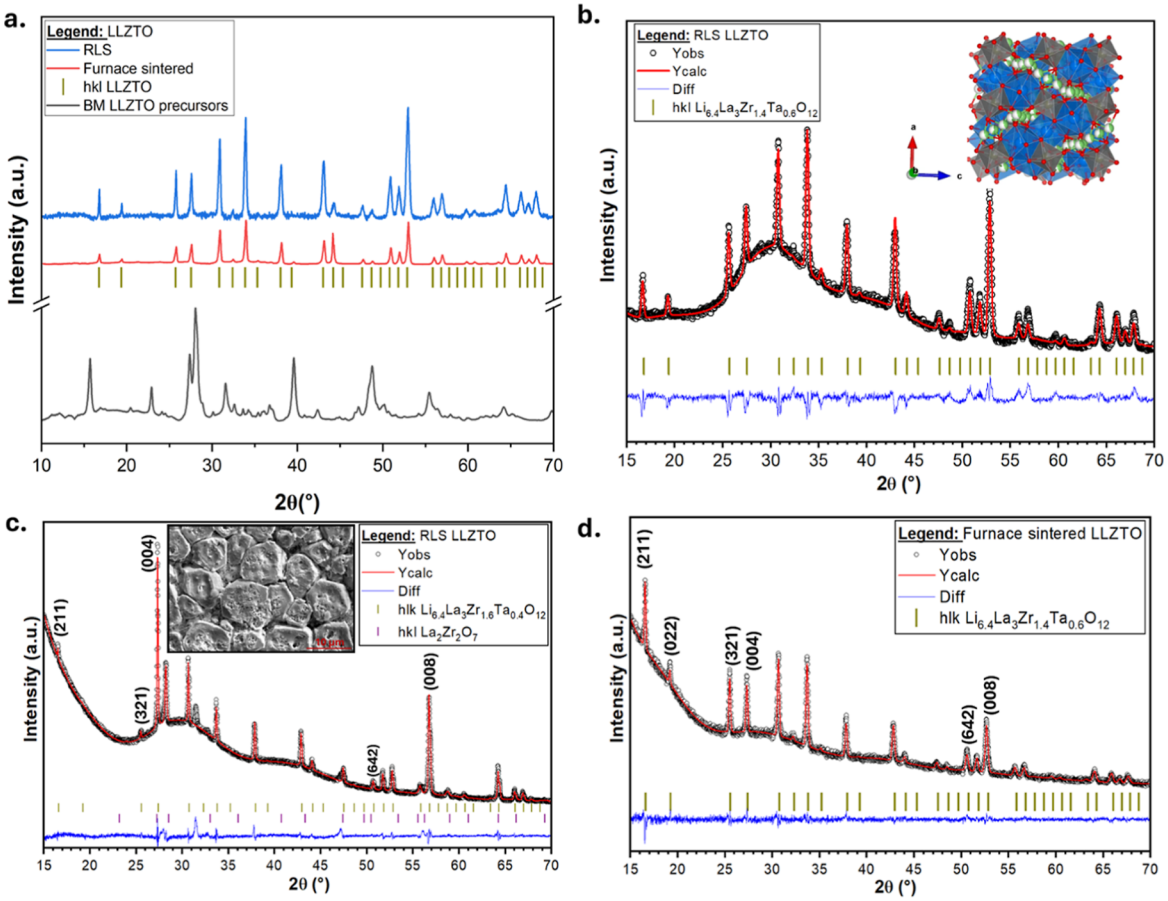

Figure 6. (a) X-ray diffraction patterns of ball-milled LLZTO precursors, furnace sintered LLZTO, and reactive laser sintering (RLS) LLZTO (AED: 1.67 J mm^{-2}); (b) Rietveld refinement of the RLS LLZTO sample processed at an areal laser energy density of 1.67 J mm^{-2} yielded agreement factors (R_{exp} = 2.28, R_{wp} = 3.93, R_p = 2.88, GOF = 1.72). An inset representation of the refined cubic crystal structure is also shown. (c) Rietveld refinement of the RLS LLZTO sample processed at an areal laser energy density of 2.22 J mm^{-2} indicates the presence of 90.77 wt % cubic LLZTO and 9.23 wt % $La_2Zr_2O_7$ (LZO), with refinement parameters of R_{exp} = 0.99, R_{wp} = 1.93, R_p = 1.14, and GOF = 1.95. An inset SEM image of the corresponding sample is also shown; (d) Rietveld refinement of the furnace sintered LLZTO R_{exp}: 3.01, R_{wp}: 2.28, R_p: 2.10, GOF: 1.32. Black circles represent the experimental data points, the red line denotes the calculated pattern, and the difference curve is shown in blue.

Table 1. Atomic Coordinates, Site Occupation Factor, and Isotropic Displacement Parameters of Reactive Laser Sintering $Li_{6.4}La_3Zr_{1.4}Ta_{0.6}O_{12}$[a]

	chemical formula			$Li_{6.46}La_3Zr_{1.466(116)}Ta_{0.522(62)}O_{12}$		
	crystal system			cubic		
	space group			$Ia\bar{3}d$ (no. 230)		
	lattice parameters			$a = b = c$ = 12.9363(59) Å, V = 2164.88 (30) Å^3, Z = 8		
atom	Wyckoff site	x	y	Z	SOF	U (eq) (Å^2)
O1	*96h*	0.09198(92)	0.1877(10)	0.28902(79)	1	**0.00899**
Ta1	*16a*	0	0	0	0.261(31)	**0.00470**
Zr1	*16a*	0	0	0	0.733(58)	**0.00470**
La1	*24c*	1/4	1/8	0	1	**0.00650**
Li1	*96h*	0.0892(70)	0.2049(76)	0.3873(83)	0.4	**0.01900**
Li2	*24d*	1/4	3/8	0	0.56	**0.01200**

[a]After the scale factor, Chebyshev background, peak shape, lattice parameters, and atomic positions were refined. The SOFs and atomic displacements parameters were fixed.

roughening and edge rounding, further supporting enhanced localized melting at elevated laser energy density. Together, these results demonstrate that laser processing parameters strongly influence phase stability, microstructure, and crystallographic texture, highlighting the tunability of the RLS approach.

The Williamson–Hall (W–H) method using the Uniform Deformation Model (UDM)[71] was employed to estimate the crystallite size and lattice microstrain of the RLS and furnace-sintered LLZTO samples, with the corresponding plots shown in Figure 7a,b. In this approach, peak broadening is assumed to originate from the combined contributions of finite crystallite size and lattice strain, following the relation

https://doi.org/10.1021/acsami.6c05262
ACS Appl. Mater. Interfaces 2026, 18, 37654–37665

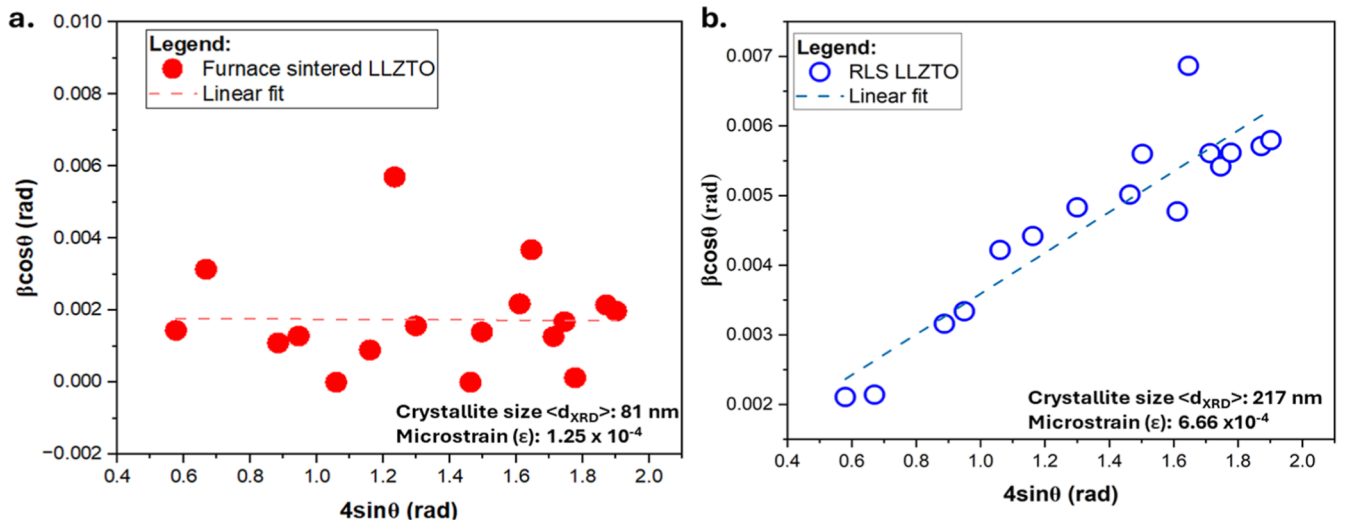

Figure 7. Williamson–Hall plots in the uniform deformation model of LLZTO samples. (a) furnace-sintered; and (b) reactive laser sintering LLZTO.

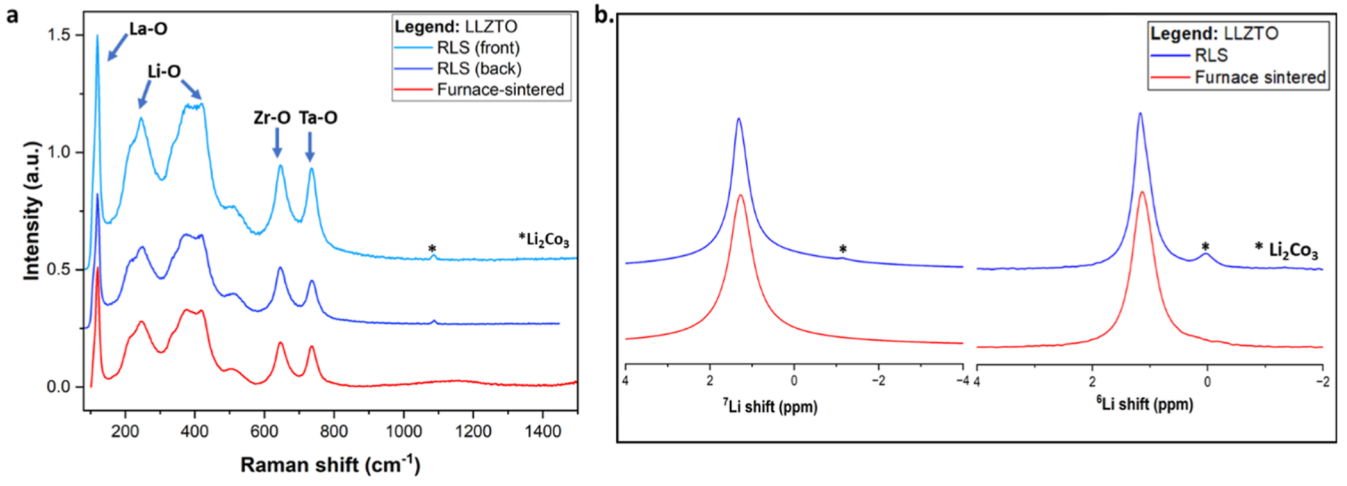

Figure 8. Characterization of furnace-sintered and reactive laser sintering LLZTO. (a) Raman spectra of both samples, collected on the front and back of the RLS pellet; and (b) solid-state ^{6}Li and ^{7}Li NMR spectra of both samples.

$$\beta\cos\theta = \frac{k\lambda}{D} + 4\varepsilon\sin\theta$$

where β is the full width at half-maximum (fwhm) after instrumental broadening correction, θ is the Bragg angle, D is the crystallite size, and ε is the lattice microstrain. The analysis was performed assuming isotropic lattice deformation and Lorentzian peak broadening, consistent with previous reports employing the UDM Williamson–Hall approach for defect and strain analysis in oxide nanomaterials. Although the method provides an approximate estimation of crystallite size and microstrain, it remains useful for comparative analysis between samples processed under identical experimental conditions.

Compared to the furnace-sintered sample, RLS LLZTO exhibits a significantly larger crystallite size (217 nm vs 82 nm), indicative of enhanced grain coarsening under ultrafast laser processing conditions. However, the RLS sample also exhibits a higher lattice microstrain than the furnace-sintered counterpart, as determined from the slope of the Williamson–Hall plots (Figure 7) (6.66×10^{-4} for RL LLZTO vs, 1.25×10^{-4} for furnace-sintered LLZTO). The increased microstrain in the RLS sample likely originates from the extreme thermal gradients and rapid melt–quench dynamics associated with localized laser heating, which can introduce residual lattice distortions and nonequilibrium structural defects.

Figure 8a shows the Raman spectra of furnace-sintered and RLS LLZTO samples. All peaks of both samples can be indexed to the cubic LLZTO phase (c-LLZTO). Raman was collected on both sides of the RLS LLZTO pellet (front and back) to verify film homogeneity. In the spectra, a narrow band in the low-frequency region (<200 cm^{-1}) corresponds to La cation vibrations. Vibrational modes below 300 cm^{-1} are associated with the LiO_6 octahedral units (96h Li1 position), while bending modes between 300 and 550 cm^{-1} are assigned to the LiO_4 tetrahedral units (24d Li2 position). The peaks at ~648 and ~736 cm^{-1} are attributed to the stretching modes of ZrO_6 and TaO_6 octahedra (16a positions), consistent with previous reports. In contrast to XRD, Raman spectroscopy detects a small signal at 1100 cm^{-1} in the RLRS LLZTO sample, assignable to Li_2CO_3 present at very low concentration -below the detection limit of XRD. Given the surface sensitivity of Raman, this signal likely arises from Li_2CO_3 located at the pellet surface, either due to brief exposure to air during

https://doi.org/10.1021/acsami.6c05262
ACS Appl. Mater. Interfaces 2026, 18, 37654–37665

handling or storage. The presumably low concentration of Li_2CO_3 in the RLS LLZTO sample is not expected to significantly impact its ionic conductivity, as discussed below.

Complementary ^6Li and ^7Li solid-state nuclear magnetic resonance (NMR) spectra (Figure 8b) confirm the formation of c-LLZTO, with dominant peaks corresponding to the cubic phase. In addition, a minor upfield peak is observed, consistent with a nonionically conductive Li species, likely Li_2CO_3. Although NMR is generally a bulk-sensitive technique, small amounts of surface Li_2CO_3 adsorbed on grain boundaries can also produce detectable signals, explaining the correlation with Raman. While CO_2 laser processing has been shown to decompose surface Li_2CO_3,[58] this aspect is beyond the scope of the present study.

The ion transport behavior of both RLS and furnace-sintered LLZTO samples was investigated by AC impedance spectroscopy. Figure 9a,b present the Nyquist plots collected at 30 °C for the furnace-sintered and RLS LLZTO samples, respectively. Both spectra consist of a high-frequency semicircle followed by a low-frequency Warburg tail, characteristic of predominantly ionic conduction. The ionic conductivity of both samples follows Arrhenius behavior over the investigated temperature range, and the corresponding activation energies for Li^+ diffusion were extracted from the linear fits shown in Figure 9c. Full temperature-dependent impedance spectra (30−80 °C) are provided in the insets of Figure 9a,b.

The RLS LLZTO exhibits a slightly higher ionic conductivity than the furnace-sintered sample, reaching 0.36 ± 0.08 mS cm^{-1} compared to 0.23 ± 0.12 mS cm^{-1}, while both samples display similar activation energies (0.41 eV for RLS LLZTO and 0.42 eV for furnace-sintered LLZTO). These conductivity values are comparable to those reported for Ta-doped LLZTO films fabricated via ultrafast Joule-heated carbon strip sintering, which typically exhibit ionic conductivities in the range of 0.1−1 mS cm^{-1}.[72] Although separate bulk and grain-boundary resistances could not be fully deconvoluted due to overlap of the impedance semicircles within the measured temperature range, the improved conductivity of the RLS sample is consistent with its higher relative density and larger crystallite size, both of which reduce grain-boundary resistance and facilitate Li^+ transport. Notably, despite exhibiting slightly higher lattice microstrain than the furnace-sintered sample, the RLS LLZTO still demonstrates superior ionic conductivity, indicating that the beneficial effects of enhanced densification and crystallite coarsening outweigh the moderate increase in lattice distortion. Collectively, these results demonstrate that reactive laser sintering enables favorable microstructural evolution for Li^+ transport while minimizing prolonged thermal exposure and lithium volatilization, highlighting RLS as a promising ultrafast processing strategy for high-performance garnet solid electrolytes.

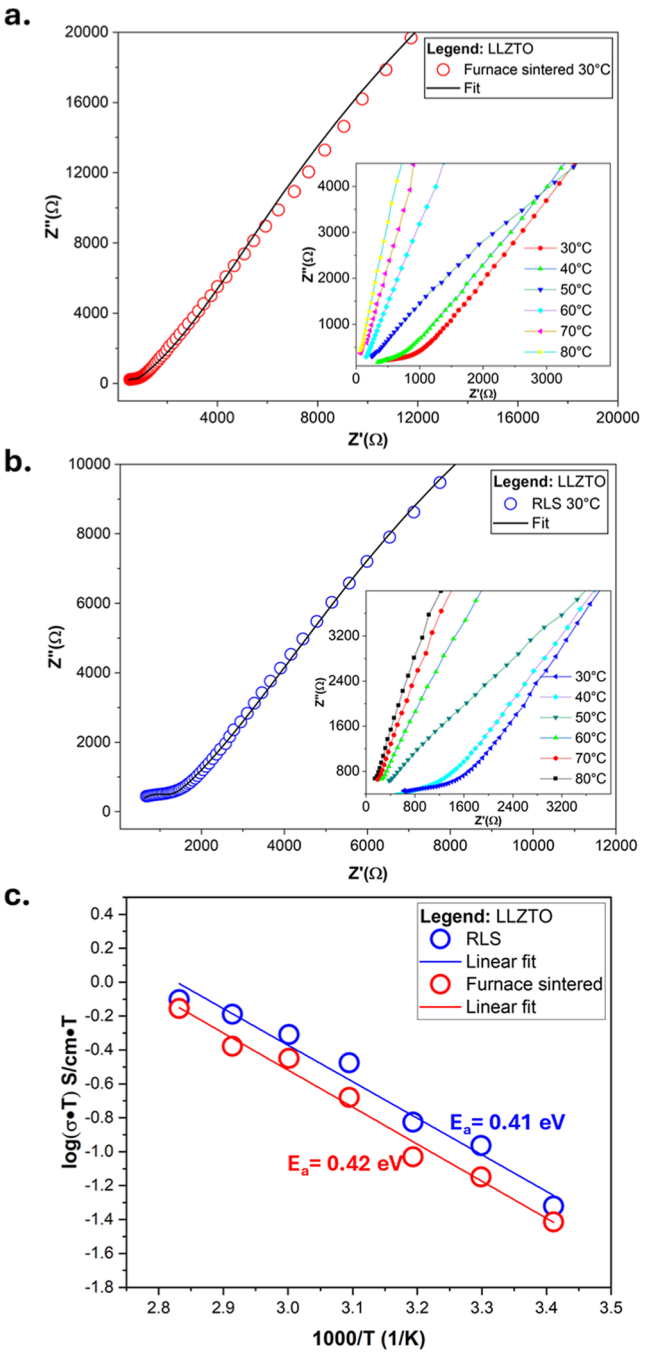

Figure 9. AC impedance analysis of LLZTO samples. Nyquist plots of (a) furnace-sintered; (b) reactive laser sintering LLZTO; insets show full temperature-dependent Nyquist spectra (30−80 °C); and (c) Arrhenius plots of ionic conductivity and extracted activation energies.

3. CONCLUSION

In this work, we demonstrate that reactive laser sintering (RLS) provides a rapid and scalable route for fabricating LLZTO solid electrolytes through simultaneous phase formation and densification. Compared with conventional furnace sintering, RLS enables ultrafast densification on subsecond time scales, achieving ∼95% relative density while minimizing lithium loss and limiting secondary phase formation. Comprehensive characterization by SEM, EDS, X-ray diffraction (XRD), Raman spectroscopy, and solid-state $^6Li/^7Li$ NMR confirms the formation of cubic garnet LLZTO with homogeneous microscale elemental distribution and dense microstructures.

Microstructural analysis reveals that RLS promotes significantly larger grain and crystallite sizes relative to furnace-sintered LLZTO, consistent with enhanced densification and reduced grain-boundary density. Although the RLS samples exhibit slightly higher lattice microstrain, they demonstrate improved ionic conductivity (0.36 mS cm^{-1}) compared to conventionally sintered samples (0.23 mS cm^{-1}), indicating that the beneficial effects of densification and grain coarsening outweigh the moderate increase in lattice distortion. In addition, nanoindentation measurements show that RLS

https://doi.org/10.1021/acsami.6c05262
ACS Appl. Mater. Interfaces 2026, 18, 37654−37665

preserves the mechanical integrity of the garnet framework despite the highly localized ultrafast thermal processing conditions.

Overall, reactive laser sintering integrates phase formation, densification, and microstructural control into a single ultrafast processing step, establishing a promising manufacturing strategy for garnet-type solid electrolytes. Beyond improving LLZTO processing efficiency and electrochemical performance, this approach provides a pathway toward scalable and high-throughput fabrication of oxide solid electrolytes for next-generation solid-state batteries.

4. EXPERIMENTAL SECTION

4.1. Synthesis

$LiOH{\cdot}H_2O$ (battery grade, Sigma-Aldrich), La_2O_3 (99.99%, Sigma-Aldrich), ZrO_2 (99.7%, Sigma-Aldrich), Ta_2O_5 (Sigma-Aldrich) and 5 wt % excess of $LiOH{\cdot}H_2O$ -for compensating lithium loss during sintering-were weighed in stoichiometric ratios and ball milled using a using a zirconia milling jar (SPEX SamplePrep) in isopropanol at 1700 rpm for 1 h with 3 mm yttria-stabilized zirconia (YSZ) beads (1:14 ball to powder ratio). The powder was pressed at 15 MPa for 2−3 min to form pellets for RLS. The RLS LLZTO was annealed using a CO_2 laser with wavelength λ = 10.6 μm, maximum power of 20 W and a Gaussian focal diameter of 1.5 mm. Samples were placed on a graphite foil in a chamber with continuous Argon gas purging and a resistive heating stage (1″ in diameter effective heating area). Stage heating was controlled by increasing the current through a Labview program. The ramping rate was approximately 30 °C/min. Once the stage temperature reached 1000 °C, laser was turned on and scanned across the sample with speed controlled by scanning galvo mirror system. After laser treatment, the stage was cooled down to room temperature and the sample was removed from the chamber. The reactive laser synthesis of c-LLZTO was performed using a 2 W CO_2 laser, a 1.5 mm (e^{-2}) Gaussian beam diameter, a scan speed of 4 mm s^{-1}, and a hatch spacing of 0.3 mm, corresponding to an aerial laser energy density of 1.67 J mm^{-2}. For samples processed at an energy density of 2.22 J mm^{-2}, a 2 W CO_2 laser was used with a Gaussian beam (1.5 mm e^{-2} diameter), a scan speed of 3 mm s^{-1}, and a hatch spacing of 0.3 mm. For the LLZTO samples prepared by conventional furnace methods, the pellets were sintered at 1100 °C for 6 h at a heating rate of 5 °C·min^{-1}.

4.2. Nanoindentation Measurements

iO4 Femto-indenter equipped with Diamond Berkovich tip was used to conduct nanoindentation experiments on reactive laser sintered and furnace sintered LLZTO samples. Both samples were mechanically polished with sandpapers up to grid #1200 in the final step. Both polishing and indentation were carried out inside an Ar-filled glovebox to avoid Li_2CO_3 surface layer formation due to air exposure. Reduced modulus and hardness values were reported for 0.9−1.1 μm contact depth range, averaging 25 data sets.

4.3. X-ray Diffraction and Raman Characterization

X-ray diffraction of the reactive laser sintered and furnace sintered LLZTO samples was performed using a Bruker D8 Advanced instrument operated at 40 kV and 40 mA with Cu−Kα radiation (λ = 1.54 Å) for phase identification, Rietveld quality pattern was recorded in Bragg−Brentano geometry. The samples were prepared in a glovebox using airtight sample holders (Bruker) to maintain an argon environment during testing. Rietveld refinements of the LLZTO samples were performed using the models for the LLZTO SSE reported by Kataoka and Akimoto.[73] Rietveld refinements of the crystal structure including scale factor, Chebyshev background, peak shape, and lattice parameters, were simultaneously refined using the software package TOPAS 6(Bruker-AXS). Refinement constraints that were used were as follows: the atomic coordinates and atomic displacement parameters were fixed to be the same of those obtained from reported model. Raman spectra were collected using an inVia confocal Raman microscope (Renishaw) equipped with a 633 nm He−Ne laser for excitation. The laser was focused onto the sample surface through a 50× objective lens. Spectra were acquired over the range of 100−1400 cm^{-1} with an acquisition time of 10 s per scan, and multiple accumulations were averaged to improve signal-to-noise ratio. The spectrometer was calibrated using the Si reference peak at 520.7 cm^{-1} prior to measurements. Data processing, including baseline correction and peak fitting, was performed using Renishaw WiRE software. Crystallite size and lattice microstrain were estimated using the Williamson−Hall (W−H) method within the Uniform Deformation Model (UDM). Unlike the Debye−Scherrer approach, the W−H method accounts for peak broadening contributions from both finite crystallite size and lattice strain. In the UDM approach, plots of $\beta \cos\theta$ versus 4 $\sin\theta$ were linearly fitted, where the slope corresponds to the lattice microstrain (ε) and the y-intercept was used to calculate the crystallite size (D) of the RLS LLZTO and furnaced sintered LLZTO samples.

4.4. Electrochemical Impedance Spectroscopy

The reactive laser sintered and furnace sintered LLZTO samples were first treated according to the method reported by Ruan et al.[74] Each LLZTO sample was first immersed in a solution of phosphoric acid and ethanol (1:1 vol ratio) for 3 min to convert any Li_2CO_3 on the surface into Li_3PO_4. The sample was then washed with ethanol twice for 2 min each and dried under vacuum for 20 min before assembling into a cell in an argon-filled glovebox. Each side of the LLZTO pellets was coated with silver paint to establish electronic contact. No external stack pressure was applied during conductivity measurements for either the laser-sintered or furnace-sintered samples. AC impedance spectroscopy was carried out using a VMP3 potentiostat/galvanostat (Bio-Logic Science Instruments) over a frequency range of 1 Hz to 1 MHz. Ionic conductivity (σ) was calculated using $\sigma = t/(RA)$, where R is the bulk resistance extracted from the high-frequency intercept, t is the pellet thickness, and A is the electrode area. The impedance spectra were fitted using the equivalent circuit R1 + C1/R2 + C2/R3 + Wd, where R1 represents the bulk resistance of the pellet, C1 and R2 account for the grain-boundary capacitance and resistance, C2 and R3 model interfacial or surface contributions, and Wd3 corresponds to a Warburg element representing ion diffusion within the material. The use of silver paste to establish electronic contact may contribute to the interfacial response captured by the circuit. Activation energies were determined from Arrhenius analysis of the temperature-dependent conductivity.

4.5. Scanning Electron Microscopy

The microstructure of the furnace-sintered and laser-sintered LLZTO samples was characterized using a scanning electron microscope (SEM). Samples were mounted on aluminum stubs using conductive carbon tape. Top-view and cross-sectional images were acquired to evaluate grain morphology, grain boundaries, and porosity. Grain size analysis was performed using ImageJ software. Individual grains were manually or semiautomatically outlined, and the area of each grain was measured to generate histograms of grain size distributions. Cross-sectional samples of furnace-sintered and laser-sintered (RLS) LLZTO pellets were prepared by ion milling to expose smooth surfaces for SEM imaging. A few representative samples were analyzed for each sintering approach, and multiple regions were imaged per sample to ensure statistical relevance. Porosity was estimated from the SEM images by outlining visible pores in ImageJ, measuring their areas, and calculating the ratio of total pore area to the total analyzed area. The relative density of each sample was then calculated as 100% minus the porosity, and the average values were determined for each sintering method.

4.6. Ar Ion Milling

Samples were prepared for SEM imaging using a JEOL Ar ion mill. The samples were fractured to expose a clean surface and then mounted onto a Si chip with carbon tape. An accelerating voltage of 6 kV was used with an ion current between 100 and 150 μA. Milling was alternated on/off for 10 s/10 s, respectively, using a total milling time of 1 h to lower the sample temperature during milling. The ion

https://doi.org/10.1021/acsami.6c05262
ACS Appl. Mater. Interfaces 2026, 18, 37654−37665

milling resulted in a milled area with a width approximately 400 μm across the thickness of the sample.

4.7. Solid-State NMR Spectroscopy

Solid-state ^{6}Li and ^{7}Li NMR spectroscopy was performed on a Bruker Avance III 400 MHz NMR spectrometer equipped with a 4 mm double-resonance magic-angle spinning (MAS) probe. Samples were packed into 4 mm zirconia rotors and spun at a MAS frequency of 12 kHz to minimize anisotropic broadening. Single-pulse experiments were conducted using a $\pi/2$ pulse length of 2.5 μs (^{7}Li) and 3.0 μs (^{6}Li), a recycle delay of 2 s, and 256−1024 scans depending on signal intensity. Chemical shifts were referenced to 1 M LiCl aqueous solution at 0 ppm. All spectra were processed using Bruker TopSpin software, with baseline correction and phase adjustment applied.

■ ASSOCIATED CONTENT

Supporting Information

The Supporting Information is available free of charge at https://pubs.acs.org/doi/10.1021/acsami.6c05262.

EDS elemental analysis of RLS LLZTO (SEM regions, spectra, and quantitative composition tables); cross-sectional SEM images of ion-milled furnace-sintered and RLS LLZTO pellets; X-ray diffraction patterns of ball-milled precursors and simulated reference phases (PDF)

■ AUTHOR INFORMATION

Corresponding Authors

Erika P. Ramos − *Materials Science Division, Lawrence Livermore National Laboratory, Livermore, California 94550, United States*; Email: ramosguzman1@llnl.gov

Jianchao Ye − *Materials Science Division, Lawrence Livermore National Laboratory, Livermore, California 94550, United States*; orcid.org/0000-0001-8939-0612; Email: ye3@llnl.gov

Authors

Yudan Chen − *Department of Chemistry & Biochemistry, Florida State University, Tallahassee, Florida 32306, United States*

Aaron Santomauro − *Department of Materials Science and Engineering, Clemson University, Clemson, South Carolina 29634, United States*

Yan-Yan Hu − *Department of Chemistry & Biochemistry, Florida State University, Tallahassee, Florida 32306, United States*

Samuel Sanghyun Lee − *Mechanical Engineering, Stanford University, Stanford, California 94305, United States*

Jianhua Tong − *Department of Materials Science and Engineering, Clemson University, Clemson, South Carolina 29634, United States*; orcid.org/0000-0002-0684-1658

Complete contact information is available at: https://pubs.acs.org/10.1021/acsami.6c05262

Notes

The authors declare no competing financial interest.

■ ACKNOWLEDGMENTS

This work was performed under the auspices of the U.S. Department of Energy by Lawrence Livermore National Laboratory under Contract DE-AC52-07NA27344 and supported by the Office of Laboratory Directed Research and Development under projects tracking codes 20-ERD-018 and 24-LW-045. Y.Y.Hu and Y.Chen thank the support from the National Science Foundation under the grant no. DMR-2319151. The solid-state NMR experiments were performed at the National High Magnetic Field Laboratory by the National Science Foundation Cooperative agreement Nos. DMR-1644779 and DMR-2128556, and the State of Florida.

■ REFERENCES

(1) Zhao, Q.; Stalin, S.; Zhao, C.-Z.; Archer, L. A. Designing Solid-State Electrolytes for Safe, Energy-Dense Batteries. *Nat. Rev. Mater.* **2020**, *5* (3), 229−252.

(2) Son, J. P.; Park, J.; Kim, H.-Y.; Kim, J.-S.; Song, Y. B.; Kim, C.; Kim, D.; Kim, J. S.; Lee, J.; Ko, S.; Jung, S.-J.; Choi, S.; Ahn, D.; Chae, K. H.; Kwon, G.; Wierzbicki, D.; Du, Y.; Lee, H.-W.; Seo, D.-H.; Nam, K.-W.; Jung, Y. S. Five-Volt-Class High-Capacity All-Solid-State Lithium Batteries. *Nat. Energy* **2025**, *10* (11), 1334−1346.

(3) Burton, M.; Narayanan, S.; Jagger, B.; Olbrich, L. F.; Dhir, S.; Shibata, M.; Lain, M. J.; Astbury, R.; Butcher, N.; Copley, M.; Kotaka, T.; Aihara, Y.; Pasta, M. Techno-Economic Assessment of Thin Lithium Metal Anodes for Solid-State Batteries. *Nat. Energy* **2025**, *10* (1), 135−147.

(4) Yang, C.; Singh, A.; Pu, X.; Mallarapu, A.; Smith, K.; Keyser, M.; Haberman, M. R.; Khani, H.; Misztal, P.; Spray, R.; Ezekoye, O. A.; Finegan, D. P. Addressing the Safety of Next-Generation Batteries. *Nature* **2025**, *645* (8081), 603−613.

(5) Zhang, W.; Wang, Z.; Wan, H.; Li, A.-M.; Liu, Y.; Liou, S.-C.; Zhang, K.; Ren, Y.; Jayawardana, C.; Lucht, B. L.; Wang, C. Revitalizing Interphase in All-Solid-State Li Metal Batteries by Electrophile Reduction. *Nat. Mater.* **2025**, *24* (3), 414−423.

(6) Wang, C.; Wu, Y.; Wang, S.; Zhu, J.; Zhuang, X. Protection of Lithium Metal Anodes: A Comprehensive Review. *J. Energy Storage* **2025**, *130*, 117454.

(7) Luo, Y.; Rao, Z.; Yang, X.; Wang, C.; Sun, X.; Li, X. Safety Concerns in Solid-State Lithium Batteries: From Materials to Devices. *Energy Environ. Sci.* **2024**, *17* (20), 7543−7565.

(8) Balaish, M.; Gonzalez-Rosillo, J. C.; Kim, K. J.; Zhu, Y.; Hood, Z. D.; Rupp, J. L. M. Processing Thin but Robust Electrolytes for Solid-State Batteries. *Nat. Energy* **2021**, *6* (3), 227−239.

(9) Han, X.; Xu, Y.; Li, H.; Wang, Z.; Yue, J.; Yan, X.; Zhang, S.; Fu, J.; Xia, Y.; Zhou, L.; Wei, S.; Liu, X.; Wang, X.; Zhao, C.; Li, X.; Bo, S.-H.; Wang, J.; Sun, X.; Liang, J. Mechanically Robust Halide Electrolytes for High-Performance All-Solid-State Batteries. *Nat. Commun.* **2025**, *16* (1), 9770.

(10) Calpa, M.; Rosero-Navarro, N. C.; Miura, A.; Tadanaga, K. Preparation of Sulfide Solid Electrolytes in the Li2S−P2S5 System by a Liquid Phase Process. *Inorg. Chem. Front.* **2018**, *5* (2), 501−508.

(11) Tsukasaki, H.; Mori, Y.; Otoyama, M.; Yubuchi, S.; Asano, T.; Tanaka, Y.; Ohno, T.; Mori, S.; Hayashi, A.; Tatsumisago, M. Crystallization Behavior of the Li2S−P2S5 Glass Electrolyte in the LiNi1/3Mn1/3Co1/3O2 Positive Electrode Layer. *Sci. Rep.* **2018**, *8* (1), 6214.

(12) Warren, Z.; Rosero-Navarro, N. C. Solution-Based Suspension Synthesis of Li2S−P2S5 Glass-Ceramic Systems as Solid-State Electrolytes: A Brief Review of Current Research. *ACS Omega* **2024**, *9* (29), 31228−31236.

(13) Park, J.-S.; Jo, C.-H.; Myung, S.-T. Comprehensive Understanding on Lithium Argyrodite Electrolytes for Stable and Safe All-Solid-State Lithium Batteries. *Energy Storage Mater.* **2023**, *61*, 102869.

(14) Wang, D.; Shi, H.; Cui, W.; Li, H.; Niu, J.; Wang, S.; Xu, Z. Li-Argyrodite Solid-State Electrolytes with Lithium Compatibility and Air Stability for All-Solid-State Batteries. *J. Mater. Chem. A* **2024**, *12* (18), 10863−10874.

(15) Tron, A.; Beutl, A.; Mohammad, I.; Paolella, A. Probing the Chemical Stability between Current Collectors and Argyrodite Li6PS5Cl Sulfide Electrolyte. *Commun. Chem.* **2025**, *8* (1), 212.

(16) Murugan, R.; Thangadurai, V.; Weppner, W. Fast Lithium Ion Conduction in Garnet-Type Li7La3Zr2O12. *Angew. Chem., Int. Ed.* **2007**, *46* (41), 7778−7781.

(17) Thangadurai, V.; Kaack, H.; Weppner, W. J. F. Novel Fast Lithium Ion Conduction in Garnet-Type Li5La3M2O12 (M = Nb, Ta). *J. Am. Ceram. Soc.* **2003**, *86* (3), 437−440.
(18) Shin, D. O.; Oh, K.; Kim, K. M.; Park, K.-Y.; Lee, B.; Lee, Y.-G.; Kang, K. Synergistic Multi-Doping Effects on the Li7La3Zr2O12 Solid Electrolyte for Fast Lithium Ion Conduction. *Sci. Rep.* **2015**, *5* (1), 18053.
(19) Enkhbayar, E.; Kim, J. Study of Codoping Effects of Ta5+ and Ga3+ on Garnet Li7La3Zr2O12. *ACS Omega* **2022**, *7* (50), 47265−47273.
(20) Ma, K.; Chen, B.; Li, C.-X.; Thangadurai, V. Improvement of the Li-Ion Conductivity and Air Stability of the Ta-Doped Li7La3Zr2O12 Electrolyte via Ga Co-Doping and Its Application in Li−S Batteries. *J. Mater. Chem. A* **2024**, *12* (6), 3601−3615.
(21) Zhao, J.; Wang, X.; Wei, T.; Zhang, Z.; Liu, G.; Yu, W.; Dong, X.; Wang, J. Current Challenges and Perspectives of Garnet-Based Solid-State Electrolytes. *J. Energy Storage* **2023**, *68*, 107693.
(22) Li, W.; Zhang, S.; Bu, X.; Luo, J.; Zhang, Y.; Yan, M.; Quan, T.; Zhu, Y. Preparation and Performance of Highly-Conductive Dual-Doped Li7La3Zr2O12 Solid Electrolytes for Thermal Batteries. *Green Energy Environ.* **2025**, *10* (2), 399−409.
(23) Muzakir, M.; Manickavasakam, K.; Cheng, E. J.; Yang, F.; Wang, Z.; Li, H.; Zhang, X.; Qin, J. Inorganic Solid Electrolytes for All-Solid-State Lithium/Sodium-Ion Batteries: Recent Developments and Applications. *J. Mater. Chem. A* **2024**, *13* (1), 73−135.
(24) Chambers, M. S.; Moy, A. C.; McMullin, L. K.; Ardrey, K. D.; Veith, G. M.; Libera, J. A.; Chen, X. C.; Armstrong, B. L. Demonstration of the Reproducibility Challenges in the Sintering Behavior of Lithium-Stuffed Garnets in Scaling up Synthesis. *Adv. Mater. Technol.* **2026**, *11* (7), No. e01803.
(25) Balaish, M.; Kim, K. J.; Chu, H.; Zhu, Y.; Gonzalez-Rosillo, J. C.; Kong, L.; Paik, H.; Weinmann, S.; Hood, Z. D.; Hinricher, J.; Miara, L. J.; Rupp, M. J. L. Emerging Processing Guidelines for Solid Electrolytes in the Era of Oxide-Based Solid-State Batteries. *Chem. Soc. Rev.* **2025**, *54* (19), 8925−9007.
(26) Zhao, J.; Wang, X.; Wei, T.; Zhang, Z.; Liu, G.; Yu, W.; Dong, X.; Wang, J. Current Challenges and Perspectives of Garnet-Based Solid-State Electrolytes. *J. Energy Storage* **2023**, *68*, 107693.
(27) Li, C.; Kern, F.; Liu, L.; Parr, C.; Börger, A.; Liu, C. Synthesis and Characterization of LLZNO & LLZTO: Insights into the Impact of Different Lithium Precursors on Properties. *Open Ceram.* **2025**, *24*, 100842.
(28) Limon, M. S. R.; Navid, A. F.; Duffee, C. W.; Ahmad, Z. Grain Boundaries in Ceramic Solid-State Lithium Metal Batteries: A Review. *Ind. Eng. Chem. Res.* **2026**, *65*, 1−26.
(29) Montoya, S. T.; Shanto, S. A. H.; Walker, R. A. Lithium Volatilization and Phase Changes during Aluminum-Doped Cubic Li6.25La3Zr2Al0.25O12 (c-LLZO) Processing. *Crystals* **2024**, *14* (9), 795.
(30) Zhao, H.; Du, M.; Mo, H.; Wang, C.; Zhou, W.; Liao, K.; Shao, Z. Garnet-Based Solid Li-Metal Batteries Operable under High External Pressure with HCOOH-Induced Electron-Blocking and Lithiophilic Interlayer. *ACS Appl. Mater. Interfaces* **2024**, *16* (34), 44997−45005.
(31) Guo, C.; Shen, Y.; Mao, P.; Liao, K.; Du, M.; Ran, R.; Zhou, W.; Shao, Z. Grafting of Lithiophilic and Electron-Blocking Interlayer for Garnet-Based Solid-State Li Metal Batteries via One-Step Anhydrous Poly-Phosphoric Acid Post-Treatment. *Adv. Funct. Mater.* **2023**, *33* (10), 2213443.
(32) Zhao, H.; Mo, H.; Mao, P.; Ran, R.; Zhou, W.; Liao, K. Tape-Casting Fabrication Techniques for Garnet-Based Membranes in Solid-State Lithium-Metal Batteries: A Comprehensive Review. *ACS Appl. Mater. Interfaces* **2024**, *16* (50), 68772−68793.
(33) Huang, L.-H.; Li, C.-C. Liquid Metallic Ga as Sintering Aid to Promote the Densification of Garnet Electrolytes for All-Solid-State Li-Ion Batteries. *J. Power Sources* **2023**, *556*, 232527.
(34) Jalem, R.; Rushton, M. J. D.; Manalastas, W., Jr.; Nakayama, M.; Kasuga, T.; Kilner, J. A.; Grimes, R. W. Effects of Gallium Doping in Garnet-Type Li7La3Zr2O12 Solid Electrolytes. *Chem. Mater.* **2015**, *27* (8), 2821−2831.
(35) Ni, K.-H.; Chen, Z.-L.; Li, C.-C. Densification and Stress Distribution within the Sintered Structure of Ceramic Electrolytes for All-Solid-State Li-Ion Batteries. *Acta Mater.* **2024**, *275*, 120057.
(36) Weller, J. M.; Chan, C. K. Pyrochlore Nanocrystals as Versatile Quasi-Single-Source Precursors to Lithium Conducting Garnets. *J. Mater. Chem. A* **2020**, *8* (34), 17405−17410.
(37) Guo, J.; Weller, J. M.; Yang, S.; Bhat, M. H.; Chan, C. K. Reactive Sintering of Garnet-Type Li6.4La3Zr1.4Ta0.6O12 (LLZTO) from Pyrochlore Precursors Prepared Using a Non-Aqueous Sol−Gel Method. *Ionics* **2023**, *29* (2), 581−590.
(38) Badami, P.; Weller, J. M.; Wahab, A.; Redhammer, G.; Ladenstein, L.; Rettenwander, D.; Wilkening, M.; Chan, C. K.; Kannan, A. N. M. Highly Conductive Garnet-Type Electrolytes: Access to Li6.5La3Zr1.5Ta0.5O12 Prepared by Molten Salt and Solid-State Methods. *ACS Appl. Mater. Interfaces* **2020**, *12* (43), 48580−48590.
(39) Weller, J. M.; Whetten, J. A.; Chan, C. K. Synthesis of Fine Cubic Li7La3Zr2O12 Powders in Molten LiCl−KCl Eutectic and Facile Densification by Reversal of Li+/H+ Exchange. *ACS Appl. Energy Mater.* **2018**, *1* (2), 552−560.
(40) Shen, F.; Guo, W.; Zeng, D.; Sun, Z.; Gao, J.; Li, J.; Zhao, B.; He, B.; Han, X. A Simple and Highly Efficient Method toward High-Density Garnet-Type LLZTO Solid-State Electrolyte. *ACS Appl. Mater. Interfaces* **2020**, *12* (27), 30313−30319.
(41) Ping, X.; Zheng, Q.; Meng, B.; Lin, W.; Chen, Y.; Fang, C.; Zhang, H.; Liang, W. Influence of Sintering Atmosphere on the Phase, Microstructure, and Lithium-Ion Conductivity of the Al-Doped Li7La3Zr2O12 Solid Electrolyte. *Ceram. Int.* **2022**, *48* (18), 25689−25695.
(42) Raju, M. M.; Altayran, F.; Johnson, M.; Wang, D.; Zhang, Q. Crystal Structure and Preparation of Li7La3Zr2O12 (LLZO) Solid-State Electrolyte and Doping Impacts on the Conductivity: An Overview. *Electrochem* **2021**, *2* (3), 390−414.
(43) Pan, H.; Fan, L.; Zhang, Y.; Zhang, L.; Shi, Y.; Xie, J.; Lei, F. A Rapid Pressureless Sintering Strategy for LLZTO Ceramic Solid Electrolyte Sheets Prepared by Tape Casting. *Solid State Ionics* **2024**, *417*, 116708.
(44) Olevsky, E. A.; Rolfing, S. M.; Maximenko, A. L. Flash (Ultra-Rapid) Spark-Plasma Sintering of Silicon Carbide. *Sci. Rep.* **2016**, *6* (1), 33408.
(45) Trapp, J.; Kieback, B. Fundamental Principles of Spark Plasma Sintering of Metals: Part I − Joule Heating Controlled by the Evolution of Powder Resistivity and Local Current Densities. *Powder Metall.* **2019**, *62* (5), 297−306.
(46) Manière, C.; Lee, G.; Olevsky, E. A. All-Materials-Inclusive Flash Spark Plasma Sintering. *Sci. Rep.* **2017**, *7* (1), 15071.
(47) Zhang, H.; Klimpel, M.; Wieczerzak, K.; Dubey, R.; Okur, F.; Michler, J.; Jeurgens, L. P. H.; Chernyshov, D.; van Beek, W.; Kravchyk, K. V.; Kovalenko, M. V. Unveiling Surface Chemistry of Ultrafast-Sintered LLZO Solid-State Electrolytes for High-Performance Li-Garnet Solid-State Batteries. *Chem. Mater.* **2024**, *36* (22), 11254−11263.
(48) Kermani, M.; Dong, J.; Biesuz, M.; Linx, Y.; Deng, H.; Sglavo, V. M.; Reece, M. J.; Hu, C.; Grasso, S. Ultrafast High-Temperature Sintering (UHS) of Fine Grained α-Al2O3. *J. Eur. Ceram. Soc.* **2021**, *41* (13), 6626−6633.
(49) Wang, C.; Ping, W.; Bai, Q.; Cui, H.; Hensleigh, R.; Wang, R.; Brozena, A. H.; Xu, Z.; Dai, J.; Pei, Y.; Zheng, C.; Pastel, G.; Gao, J.; Wang, X.; Wang, H.; Zhao, J.-C.; Yang, B.; Zheng, X.; Luo, J.; Mo, Y.; Dunn, B.; Hu, L. A General Method to Synthesize and Sinter Bulk Ceramics in Seconds. *Science* **2020**, *368* (6490), 521−526.
(50) Kotobuki, M.; Koishi, M. High Conductive Al-Free Y-Doped Li7La3Zr2O12 Prepared by Spark Plasma Sintering. *J. Alloys Compd.* **2020**, *826*, 154213.
(51) Fukuda, M.; Li, Y.; Wei, J.; Harata, K.; Luo, G.; Snyder, G. J.; Sato, Y. S.; Kato, H.; Cheng, E. J. High-Temperature Sintering of Garnet Solid Electrolyte Li7La3Zr2O12: A Comparative Study of

https://doi.org/10.1021/acsami.6c05262
ACS Appl. Mater. Interfaces 2026, 18, 37654−37665

Induction Hot Pressing and Spark Plasma Sintering. *Small* **2025**, *21* (41), No. e06257.
(52) Wang, R.; Ping, W.; Wang, C.; Liu, Y.; Gao, J.; Dong, Q.; Wang, X.; Mo, Y.; Hu, L. Computation-Guided Synthesis of New Garnet-Type Solid-State Electrolytes via an Ultrafast Sintering Technique. *Adv. Mater.* **2020**, *32* (46), No. e2005059.
(53) Guillon, O.; De Souza, R. A.; Mishra, T. P.; Rheinheimer, W. Electric-Field-Assisted Processing of Ceramics: Nonthermal Effects and Related Mechanisms. *MRS Bull.* **2021**, *46* (1), 52−58.
(54) Lieou, C. K. C.; Bronkhorst, C. A. Thermomechanical Conversion in Metals: Dislocation Plasticity Model Evaluation of the Taylor-Quinney Coefficient. *Acta Mater.* **2021**, *202*, 170−180.
(55) Li, C.; Kern, F.; Liu, L.; Parr, C.; Börger, A.; Liu, C.; Li, C.; Kern, F.; Liu, L.; Parr, C.; Börger, A.; Liu, C. Phase Formation Study of Solid-State LLZNO and LLZTO via Structural, Thermal, and Morphological Analyses. *Ceramics* **2025**, *8* (4), 132.
(56) Xiao, Y.; Wang, Y.; Bo, S.-H.; Kim, J. C.; Miara, L. J.; Ceder, G. Understanding Interface Stability in Solid-State Batteries. *Nat. Rev. Mater.* **2020**, *5* (2), 105−126.
(57) Raj, V.; Wang, Y.; Feng, M.; Naik, K. G.; Jain, M.; Vishnugopi, B. S.; Deng, S.; Schorr, N. B.; Salazar, M.; Heusser, A. M.; Huang, X.; Manning, A. S.; Kalnaus, S.; Liu, Y.; Watt, J.; McBrayer, J. D.; Boyce, B. L.; Fang, H.; Jena, P.; Mukherjee, P. P.; Qi, Y.; Mitlin, D. Grain Boundary Zirconia-Modified Garnet Solid-State Electrolyte. *Nat. Mater.* **2025**, *25*, 249−258.
(58) Ramos, E.; Browar, A.; Roehling, J.; Ye, J. CO2 Laser Sintering of Garnet-Type Solid-State Electrolytes. *ACS Energy Lett.* **2022**, *7* (10), 3392−3400.
(59) Fu, K.; Gong, Y.; Hitz, G. T.; McOwen, D. W.; Li, Y.; Xu, S.; Wen, Y.; Zhang, L.; Wang, C.; Pastel, G.; Dai, J.; Liu, B.; Xie, H.; Yao, Y.; Wachsman, E. D.; Hu, L. Three-Dimensional Bilayer Garnet Solid Electrolyte Based High Energy Density Lithium Metal−Sulfur Batteries. *Energy Environ. Sci.* **2017**, *10* (7), 1568−1575.
(60) Krauskopf, T.; Hartmann, H.; Zeier, W. G.; Janek, J. Toward a Fundamental Understanding of the Lithium Metal Anode in Solid-State Batteries-An Electrochemo-Mechanical Study on the Garnet-Type Solid Electrolyte Li6.25Al0.25La3Zr2O12. *ACS Appl. Mater. Interfaces* **2019**, *11* (15), 14463−14477.
(61) Pelz, J. S.; Ku, N.; Meyers, M. A.; Vargas-Gonzalez, L. R. Additive Manufacturing of Structural Ceramics: A Historical Perspective. *J. Mater. Res. Technol.* **2021**, *15*, 670−695.
(62) Dzogbewu, T. C.; de Beer, D. J. Direct Laser Powder Bed Fusion of Ceramics. *Results Mater.* **2025**, *25*, 100664.
(63) Yang, Y.; Ragnvaldsen, O.; Bai, Y.; Yi, M.; Xu, B.-X. 3D Non-Isothermal Phase-Field Simulation of Microstructure Evolution during Selective Laser Sintering. *npj Comput. Mater.* **2019**, *5* (1), 81.
(64) Karacasulu, L.; Manière, C.; Vakifahmetoglu, C.; Marinel, S.; Biesuz, M. Sintering Under High Heating Rates. *Annu. Rev. Mater. Res.* **2025**, *55*, 203−230.
(65) German, R. M. Rapid Heating Concepts in Sintering. *J. Korean Powder Metall. Inst.* **2013**, *20* (2), 85−99.
(66) Chaim, R. Liquid Film Capillary Mechanism for Densification of Ceramic Powders during Flash Sintering. *Materials* **2016**, *9* (4), 280.
(67) Qian, B.; Shen, Z. Laser Sintering of Ceramics. *J. Asian Ceram. Soc.* **2013**, *1* (4), 315−321.
(68) German, R. M. *Sintering: From Empirical Observations to Scientific Principles*; Butterworth-Heinemann, 2014; ..
(69) Touidjine, K.; Finsterbusch-Rosen, M.; Kiyek, V.; Ganapathy, S.; Finsterbusch, M.; Guillon, O.; Huijben, M.; Kelder, E.; Wagemaker, M.; Fattakhova-Rohlfing, D. The Impact of Lithium Carbonate on Tape Cast LLZO Battery Separators: A Balanced Interplay between Lithium Loss and Relithiation. *Energy Storage Mater.* **2024**, *71*, 103487.
(70) Jonson, R. A.; Yi, E.; Shen, F.; Tucker, M. C. Optimization of Tape Casting for Fabrication of Li6.25Al0.25La3Zr2O12 Sheets. *Energy Fuels* **2021**, *35* (10), 8982−8990.
(71) Rabiei, M.; Palevicius, A.; Monshi, A.; Nasiri, S.; Vilkauskas, A.; Janusas, G. Comparing Methods for Calculating Nano Crystal Size of Natural Hydroxyapatite Using X-Ray Diffraction. *Nanomaterials* **2020**, *10* (9), 1627.
(72) Yuan, J.; Zhang, Y.; Chen, F.; Gu, Z. An Overview of Joule Heating in Energy Storage Materials and Applications. *J. Mater. Chem. C* **2024**, *12* (37), 14729−14753.
(73) Kataoka, K.; Akimoto, J. Lithium-Ion Conductivity and Crystal Structure of Garnet-Type Solid Electrolyte Li7−xLa3Zr2−xTaxO12 Using Single-Crystal. *J. Ceram. Soc. Jpn.* **2019**, *127* (8), 521−526.
(74) Ruan, Y.; Lu, Y.; Huang, X.; Su, J.; Sun, C.; Jin, J.; Wen, Z. Acid Induced Conversion towards a Robust and Lithiophilic Interface for Li−Li7La3Zr2O12 Solid-State Batteries. *J. Mater. Chem. A* **2019**, *7* (24), 14565−14574.

https://doi.org/10.1021/acsami.6c05262
ACS Appl. Mater. Interfaces 2026, 18, 37654−37665